Version of Record: https://www.sciencedirect.com/science/article/pii/S037838391730532X
Manuscript_c4daa59c9da94717f7e10ddcc2fbb3b7

Identification of storm events and contiguous coastal sections for deterministic modeling of extreme coastal flood events in response to climate change

Li H. Erikson[a], Antonio Espejo[b], Patrick L. Barnard[a], Katherine A. Serafin[c], Christie A. Hegermiller[a], Andrea O'Neill[a], Peter Ruggiero[c], Patrick W. Limber[a], and Fernando J. Mendez[d]

[a]U.S. Geological Survey (USGS), Pacific Coastal & Marine Science Center (PCMSC), 2885 Mission St., Santa Cruz, CA 95060, USA; lerikson@usgs.gov, pbarnard@usgs.gov, chegermiller@usgs.gov, aoneill@usgs.gov, plimber@usgs.gov CORRESPONDING AUTHOR: lerikson@usgs.gov

[b]IH Cantabria, Parque Científico y Tecnológico de Cantabria, C/ Isabel Torres, 15, 39011 Santander, Cantabria, Cantabria, Spain; antonio.espejo@unican.es

[c]College of Earth, Ocean, and Atmospheric Sciences, Oregon State University (OSU), Corvallis, OR 97331, USA; kserafin@coas.oregonstate.edu; pruggier@coas.oregonstate.edu

[d]Departamento Ciencias y Tecnicas del Agua y del Medio Ambiente, Universidad de Cantabria, Santander, Spain; fernando.mendez@unican.es

[e]Department of Geophysics, Stanford University, Stanford, CA, USA

Abstract

Deterministic dynamical modeling of future climate conditions and associated hazards, such as flooding, can be computationally-expensive if century-long time-series of waves, sea level variations, and overland flow patterns are simulated. To alleviate some of the computational costs, local impacts of individual coastal storms can be explored by first identifying particular events or scenarios of interest and dynamically modeling those events in detail. In this study, an efficient approach to selecting storm events for subsequent deterministic detailed modeling of coastal flooding is presented. The approach identifies locally relevant scenarios derived from regional datasets spanning long time-periods and covering large geographic areas. This is done by identifying storm events from global climate models using a robust, yet computationally simple approach for calculating total water level proxies at the shore, assuming a linear superposition of the important processes contributing to the overall total water level. Clusering of the total water level time-series is used to define coherent coastal cells where similar return period water level extrema occur in response to region-wide storms. Results show that the more severe but rare coastal flood events (e.g., the 100-year (yr) event) typically occur from the same storm across the region, but that a number of different storms are responsible for the less severe but more frequent local extreme water levels (e.g., the 1-yr event). This new 'storm selection' approach is applied to the Southern California Bight, a region of varying shoreline orientations that is subject to wave refraction across complex bathymetry, and shadowing, focusing, diffraction, and dissipation of wave energy by islands. Results indicate that wave runup dominates total water level extremes at this study site, highlighting the importance of downscaling global-scale models to nearshore waves when seeking accurate projections of local coastal hazards in response to climate change.

Keywords: coastal storm cells, dynamical downscaling, global climate models, *k*-means clustering, Southern California

1 Introduction

Flood maps are regularly used for design and hazard mitigation planning. However, until relatively recently, little information existed on probable coastal flood hazards under climate change. Changes in atmospheric conditions such as temperature, atmospheric pressure, and wind can impart deviations in both magnitude and frequency of storm events compared to the past (Graham and Diaz, 2001) which, combined with sea level rise, will affect coastal flooding projections (Sweet and Park, 2014; Barnard et al., 2014).

Scientists and coastal engineers tasked with developing flood maps typically develop 30+ year time-series of total water levels (*TWL*) using historical observations of tides, waves, and non-tidal water level fluctuations. High *TWL* events are then selected and extrapolated to extreme events by fitting probability density functions and applying extreme value theory (e.g. Allan et al., 2012). Some approaches develop an ensemble of synthetic *TWL*s time-series, taking into account conditional dependencies between tides, storm surges, and wave events in a Monte Carlo sense (Callaghan et al., 2008; Serafin and Ruggiero, 2014), while others apply a deterministic approach in which selected storm events are dynamically simulated (e.g., Barnard et al., 2014).

Future climate cannot necessarily be derived from trends of the intensity and frequency of past storms because nonlinear responses due to changing ocean temperatures and atmospheric circulation are expected (Yin, 2005; Solomon et al., 2007; Ulbrich et al., 2008; Seiler et al., 2016; Michaelis et al., 2017; Mentaschi et al., 2017). Therefore, when considering the range of possible changes in the future climate and its influence on coastal hazards, atmosphere-ocean global climate models (GCMs) are currently the best available tools for assessing different scenarios. However, the coarse resolution of GCMs limits their ability to represent local conditions that are essential for coastal impact studies (IPCC, 2007) and thus typically require downscaling of GCM fields to regional and local scales (Wood et al., 2004). A number of studies have conducted regional downscaling of GCMs for evaluation of changes in future storm surges and wave conditions (e.g., Harper et al. 2009; Smith et al 2010; Mousavi et al., 2011; Bromirski et al., 2012; Hoeke et al 2013; Camus et al., 2014; Erikson et al., 2015), but only a few have developed detailed flood hazard maps from the combined impacts of projected sea level rise, wave runup, storm surge, and other non-tidal residuals. One such study employs the Coastal Storm Modeling System (CoSMoS, Barnard et al., 2014), a predominantly deterministic approach to make detailed predictions of sea level rise and storm-induced coastal flooding over large geographic scales. The system uses the global WaveWatch III wave model, the TOPEX/Poseidon satellite altimetry-based global tide model (Egbert et al., 1994), and atmospheric forcing data from GCMs to determine regional wave and water-level boundary conditions. These physical processes are dynamically-downscaled using a series of nested SWAN and Delft3D-FLOW models linked at the coast to tightly-spaced XBeach (eXtreme Beach: Roelvink et al., 2009) cross-shore profile models. The explicit downscaling approach of CoSMoS, from a global to local scale, is computationally-expensive and therefore does not lend itself to simulating long time-series. Instead, the model system is run for scenarios of interest, such as the annual or 100-yr return level storm event in combination with a series of sea level rise scenarios. In areas of complex geography and bathymetry, special attention to local influences on water levels is necessary. For example, storm events for the CoSMoS North-Central California outer coast were selected based on offshore wave conditions, which, after accounting for cross-shelf refraction and dissipation and orientation of shoreline with respect to incident wave direction, did not systematically result in greater flood extents with increasingly-intense offshore storms (Erikson et al., in review).

Developing a robust, efficient, yet simple approach for determining relevant storm scenarios is critical for any workflow that aims to assess local-scale coastal impacts of climate change. In this paper, we present an approach to downscale global climate models for the purpose of (1) identifying locations that respond similarly to region-wide (100s of kilometers (kms)) storms and (2) selecting relevant events for evaluation of local-scale (10s of kms) coastal storm impacts. Proxies of total water levels, TWL_{px}, are computed for the 21st century assuming a linear super-position of estimated wave runup, storm surge and sea level anomalies (fig. 1). k-means clustering techniques are then used to define coastal segments where coastal storms yield TWL_{px} of similar return periods (item 2 in fig. 1). Coastal storms within each of these geographically distinct cells are identified for subsequent deterministic modeling with the Coastal Storm Modeling System, CoSMoS (Barnard et al. 2014) (item 3 in fig. 1). This new 'storm selection' approach is applied to the Southern California Bight which represents a region of varying shoreline orientations, wave transformation across complex bathymetry, and blocking, diffraction, and dissipation of wave energy by islands and immediate surrounding bathymetry (O'Reilly, 1993, Adams et al., 2008, Crosby et al., 2016). The influence of local physical settings such as these are discussed and shown to affect projected changes in future conditions relative to the past and to influence the storm selection process on a local scale. The region is heavily urbanized, with a coastal population of 18 million, and therefore an accurate assessment of future flood hazards has significant societal implications.

Figure 1. Flowchart summarizing the workflow used to determine *TWL* proxies at the coast and selecting future storm events for detailed deterministic modeling of local extreme flood events.

2 Study Area

The Southern California Bight (Southern California Bight) extends from the U.S. / Mexican border northward to Point Conception and encompasses ~500 km of partially-protected open coast shoreline (fig. 2). The active, complex tectonic setting along the Pacific and North American plate boundary has resulted in the region being fronted by a narrow continental shelf, a series of islands, pocket beaches backed by semi-resistant bedrock sea cliffs, and a highly irregular complex bathymetry that hosts a plethora of submerged seamounts, troughs, and canyons (Christiansen and Yeats 1992; Hogarth et al. 2007). The presence of seamounts, knolls, canyons, and the Channel Islands significantly alters the deep-water wave climate to a more complicated nearshore wave field (O'Reilly and Guza, 1993; O'Reilly et al., 1999; Rogers et al., 2007; Adams et al., 2008). The islands block waves approaching from many directions, yielding a large wave energy shadow zone. Additionally, complex shallow water bathymetry adjacent to the islands, seamounts, and canyons scatters, focuses, and dissipates wave energy, resulting in highly variable wave energy distribution patterns along the coast. Though swell dominates nearshore wave energy, locally-generated seas contribute ~40% to the total wave energy spectrum (Crosby et al., 2016). To account for these complexities and include contributions of both swell and local seas, the approach developed for this study employs a numerical wave model to generate a look-up table that relates offshore wave and wind parameters to nearshore wave conditions. Tides are mixed, semi-diurnal, with a microtidal diurnal range of 1.7 m (NOAA, 2017). Offshore waves can reach ~10 m during the most extreme events (CDIP, 2017), and therefore even with dissipation across the shelf, wave-driven water levels (i.e. set-up and runup) are still the dominant contributors to extreme coastal water levels across the region, while storm surge and El-Niño-driven water level anomalies rarely contribute more than ~20-30 cm each (Flick, 1998; Bromirski et al, 2003).

Figure 2. Overview of study area.

3 Data, Methods, and Models

Total water level proxies (TWL_{px}) are used as the basis for 1) identifying coastal segments that respond similarly to region-wide coastal storms and 2) selecting storm events for further detailed modeling (items 1 through 3 in fig. 1).

TWL_{px} are calculated assuming linear superposition of wave runup ($R_{2\%}$), storm surge (SS), and sea level anomalies (SLA),

$$TWL_{px} = R_{2\%} + SS + SLA \tag{1}$$

Variations in water levels due to astronomical tides are not included in Eq. (1) as they are independent of atmospheric conditions and thus should not, on a first-order basis, affect identification of coastal cells and storm events (items 2 and 3 in fig. 1). It is recognized that nearshore wave heights and $R_{2\%}$ are affected by tidal stage and currents, and that the phase of tides and storm surge can have an amplification effect on non-tidal residuals (Horsburgh and Wilson, 2007). Such variations and amplifications can be accounted for in detailed local models (e.g., CoSMoS, Barnard et al., 2014), but are assumed to be sufficiently small to not significantly affect the storm selection process presented in this work.

Conditional dependencies of $R_{2\%}$, *SS*, and *SLA* are accounted for with Eq. (1) through the use of internally-consistent boundary conditions from a single GCM. Winds, sea level pressures (SLPs), and sea surface temperatures from the National Oceanic and Atmospheric Administration (NOAA) Geophysical Fluid Dynamics Laboratory Earth System (GFDL-ESM2M) GCM are used to develop continuous time-series of $R_{2\%}$, *SS*, and *SLA*, respectively (fig. 1). These components are discussed in further detail below.

3.1 Nearshore wave and runup models

Wave runup represents the combination of wave setup caused by gradients in radiation stress due to breaking waves (e.g., Longuet-Higgins and Stewart, 1964) and swash motions across the foreshore (e.g., Hunt, 1959; Ruggiero et al., 2001). Wave runup can be empirically related to deep-water wave conditions. For the purpose of calculating TWL_{px}, the Stockdon et al. (2006) formulation is used to compute the 2% exceedance percentile of extreme runup:

$$R_{2\%} = 1.1\left(0.35\beta_f(SWH \cdot L_o)^{1/2} + 0.5 \cdot \left[SWH \cdot L_o\left(0.563\beta_f^2 + 0.004\right)\right]^{1/2}\right) \qquad (2)$$

where β_f is the beach slope, *SWH* is the significant wave height, and L_o is the deep-water wave length, $L_o = gT_p^2/2\pi$, T_p is the peak wave period, and *g* is acceleration due to gravity. A representative slope of $\beta_f = 0.03$ was used for all $R_{2\%}$ calculations. Foreshore slopes were calculated at 4,802 tightly-spaced (~100 m in the along-shore direction) cross-shore profiles that were extracted from a seamless digital elevation model (Danielson et al. 2016). Slopes were derived between 0.8 m above and below the intersection of MSL following the method described in Stockdon et al. (2006) (two times the standard deviation of the varying water level) and using observation data at Ocean Beach, CA (Erikson et al., 2007). Foreshore slopes of all Southern California Bight transects, excluding vertical cliffs, range from near flat to 0.83 with a mean and standard deviation of 0.03 ± 0.04. This region-wide representative mean slope was used in this work so that local storm intensities could be compared equally across the region independent of local seasonal and short-term variations and changes in foreshore slopes.

SWH and L_o in Eq. (2) are typically taken as back-shoaled deep-water conditions that are assumed to have accounted for energy loss due to continental shelf refraction and sheltering by objects such as islands, making it a highly site-specific computation for the Southern California Bight. The complex bathymetry and wave energy shadowing significantly alter nearshore wave conditions compared to what they might be along an open, unobstructed coastline, as assumed in Eq. (2) and other empirical runup formulae. Thus, it is necessary to deterministically transform deep-water waves to the nearshore. This was done with stationary SWAN (Simulating Waves

Nearshore, Delft University of Technology) wave model runs. SWAN is a third-generation spectral wave model specifically developed for the nearshore and includes wave growth, propagation, nonlinear wave-wave interactions, refraction, dissipation, and depth-induced breaking (Booij et al., 1999; Ris et al., 1999).

Transformation of deep water waves to the nearshore

A curvilinear SWAN model grid from the U.S./Mexican border to north of Pt. Conception was created (fig. 2). The offshore extent was defined by locations of U.S. Army Corps of Engineers Wave Information Study (WIS; *http://wis.usace.army.mil/*) points located approximately 25 km offshore; hindcast time-series of the bulk parameter triplets, SWH, T_p, and wave direction, D_p from 17 WIS output locations were applied at the open boundaries (red filled circles in fig. 2). WIS time-series used in this study are shoreward of the Channel Islands (fig. 2), and include shadowing effects as they are output from a larger model. WIS station bulk forcing parameters were interpolated at SWAN grid cells that fell between the WIS output points, thus assuming linear spatial transitions along sections of the open boundary. An exception to this was along the northern and southern lateral boundaries where bulk parameter forcings from the most northerly and southerly WIS points were applied uniformly. Although uncertain, it is recognized that the WIS outputs points may not be spaced finely enough to adequately capture the spatial heterogeneity of the wave field that passes through the complex offshore topography and islands. An additional shortcoming of the SWAN model setup lies in the use of bulk parameters rather than full 2D spectra. The Southern California Bight is subject to wave energy from multiple generation sources that arrive simultaneously and often result in multi-modal wave spectra (Hegermiller et al. 2017; Kumar et al. 2017); these multiple swell energy peaks were not captured with the bulk parameter forcings applied at the open boundaries.

Additional wave energy from locally generated seas were accounted for by applying, across the entire SWAN domain, spatiotemporally-varying near-surface (10 m height) wind fields from the 10km California Reanalysis Downscaling (CaRD10; Kanamitsu and Kanamaru, 2007; SIO 2015a) database. Hindcast simulations and testing of model skill were done using the same CaRD10 database covering years 1980-2010 (Hegermiller et al., 2016).

Horizontal SWAN grid resolution ranged from <10 m to ~800 m with finer resolution along the coast. The grid was populated with bathymetry data from the 2013 Coastal California TopoBathy Merge Project (NOAA, 2013) and was run in a stationary mode, assuming a JONSWAP wave spectral shape, 10° directional spread, and 34 frequency bands ranging logarithmically from 0.0418 to 1 Hz. Energy dissipation due to depth-induced breaking was modeled with the Battjes and Janssen (1978) formulation, bottom friction followed the semi-empirical Hasselmann et al. (1973) JONSWAP formulation with a coefficient of 0.038 m^2s^{-3}, and whitecapping was modeled following Komen et al. (1994). Because the model was run in stationary mode and assumes fully developed seas, wave energy from local seas may be somewhat over-estimated but this was not explicitly evaluated as part of this study.

Look-up table relating deep water waves to nearshore equivalents

A look-up table was developed to relate deep water waves to nearshore points in ~10 m water depth and collocated with the offshore ends of the cross-shore transects from which foreshore slopes were computed. Three-hourly hindcast SWH, T_p, and peak wave directions ($D_{p,}$) at each of the nearshore points computed with the SWAN model were used in combination with deep-water wind and wave conditions at a single offshore point to build a look-up table. For this application, hindcasted parameter time-series from the NOAA Climate Forecast System Reanalysis Reforecast (CFSRR; Chawla et al., 2013) were used since observation time-series contains gaps and the CFSRR spans a comparatively longer time-period. The offshore CFSRR point is co-located with California Data Information Program (CDIP; Scripps Institute of Oceanography; http://cdip.ucsd.edu) buoy 067 (33.2205°N, 119.8807°W).

The look-up-table was developed by binning CFSRR deep-water wave parameters (SWH,T_p, D_p) and CaRD10 wind speed (U) at CDIP067. Significant wave height was binned from 0.5-10.25 m at 0.25 m intervals; T_p was binned from 3-24 s at 3 s intervals; D_p was binned from 5-360° at 5° intervals; and U from 0-24 m/s at 6 m/s intervals. For each combination of deep-water SWH, T_p, D_p, and U, time indices falling into each bin were identified. These time indices were used to identify the resultant SWAN modeled SWH, T_p, T_m, D_p, and D_m at each nearshore point for which median values were calculated. This was done for each of the 4,802 nearshore points and all combinations of deep water binned parameters. In this way, the look-up-table was completed by assigning wave and wind conditions at CDIP067 to SWAN-computed transformations to the nearshore that were performed with WIS boundary wave data.

The look-up-table was used in combination with 3-hourly winds from CaRD10 GFDL-ESM2M and deep water wave time-series to generate nearshore wave climatologies for the historical (1976-2005) and projected (2012-2100) time-periods. Historical and future deep-water wave time-series were computed with the WaveWatch III numerical wave model (Tolman et al., 2002; Erikson et al. 2015) driven by native resolution GFDL-ESM2M winds. Skill of the Wavewatch III GFDL-ESM2M model was evaluated by comparing historical winter (November through March) wave climatologies to observations offshore of the Southern California Bight for which results indicate an overall mean model bias (model – observed) of -0.25 m and +1 s, for SWH and T_p respectively (Erikson et al., 2015; fig. 5). While this level of accuracy is sufficient for this application, more robust computations would be achieved using an ensemble of several GCMs (e.g., Hemer et al., 2013).

For the 21st century climate change simulations, near-surface (10 m height) winds from the representative concentration pathway RCP 4.5 scenario were used. RCP 4.5 represents a medium radiative atmospheric forcing with the onset of stabilization by mid-century reaching an increase in total global radiation of +4.5 MW/m^2 by the year 2100, relative to pre-industrial (1850) conditions (Hibbard et al., 2007; Moss et al., 2010). RCP 4.5 was selected over the higher emissions scenario RCP 8.5 because it has been shown that the former projects slightly greater SWH in the vicinity of the Southern California Bight (Erikson et al., 2015).

3.2 Non-tidal residuals and decomposition of storm surge and sea level anomalies

The combination of *SS* and other sea level anomalies is often referred to as non-tidal residuals (*NTR*), which are traditionally computed as the difference between measured and predicted astronomical tides. However, produced through simple subtraction, *NTR*s can be corrupted by timing errors and datum shifts resulting in tidal energy remaining in simple *NTR* computations (Pugh, 1987; Haigh et al., 2013). Additionally, the aim here is to account for short term (hours to days) wind/pressure-induced SS and longer term (days to months) water level anomalies caused by basin-scale climate variability such as the El Niño Southern Oscillation (ENSO). Therefore, to decompose the *NTR*s into these separate components, we remove the sea level anomalies (SLA) from the water levels, and then remove the tidal signal using a slightly modified approach of the spectral method described by Bromirski et al. (2003) to produce *SS*.

Monthly mean sea levels were calculated by averaging each month of every year from de-trended, de-meaned water level observations. The seasonal cycle was then subtracted from the monthly mean sea levels. The seasonal component was obtained by fitting a multi-linear regression model to the de-trended, de-meaned data. Annual and semi-annual signals were modeled using $\alpha_1 \sin(2\pi t) + \alpha_2 \cos(2\pi t) + \alpha_3 \sin(4\pi t) + \alpha_4 \cos(4\pi t)$, where t is the time in years and α are empirical coefficients. Both the seasonal cycle and the *SLA* were removed from the water level observations, resulting in a high frequency signal. Successive two-year blocks of the remaining water levels were transformed into the frequency domain and processed with a 50% overlap. Tide bands were removed and replaced with amplitude and phase estimates consistent with the concurrent non-tide continuum (Bromirski et al., 2003; Serafin and Ruggiero, 2014). The spectrum was transformed back to the time domain and 25% of the data was removed from each end of the overlapping blocks to minimize window edge effects. This method resulted in a *SS* time-series excluding energy at tidal frequencies.

Decomposition of *NTR*s was computed from tide gauge observations at La Jolla (#9410230) and Los Angeles (#9410660) (fig. 3; Table 2), each representing the approximate south and central sections of the study area (fig. 2). The observational record length at Santa Barbara, located near the north end of the study area, was deemed too short (total of 10 years, 1996-1997 and 2005-present) to represent a full climatology, which is best represented with 30+ years of data.

Table 2. Summary statistics of hourly water level data measured at NOAA tide stations.

	Time period of record	**% missing data**	**Max storm surge (m)**	**Max SLA (m)**	**Tide range (m)**
La Jolla (9410230)	01 Aug 1924 – 31 Dec 2014	6.5	0.39 (18 Jan 1978)	0.20 (Nov 1997)	±1.13

Los Angeles (9410660)	29 Nov 1923 - 31 Dec 2014	1	0.40 (02 Mar 1983)	0.18 (Nov 1997)	±1.16

Figure 3. Measured water levels and decomposed time-series of storm surge and of mean monthly sea level anomalies.

3.3 Empirical storm surge model

Storm surge is the rise of water caused by strong onshore winds and a drop in atmospheric pressure. These long waves have characteristic timescales of several hours to one day or more and wavelengths approximately equal to the width of the storm cell, typically between 150 and 800 km (CIRIA et al., 2007).

Maximum storm surge levels were found to be 0.39 m and 0.40 m at La Jolla and Los Angeles, respectively (Table 2). The maxima are very similar at these two sites but occurred during different storms in January 1978 and March 1983 at La Jolla and Los Angeles, respectively. Both extremes are associated with El Niño events but corresponding *SS* levels were only 25% to 50% as high at the opposing site during three days preceding or following each storm, indicating significant spatial variability.

The inconsistency of *SS* response to individual storms is related to differences in storm patterns and shoreline orientation at the two sites. The La Jolla tide gauge is situated on a northwest-facing coast, whereas the Los Angeles gauge is oriented southwest (fig. 2) and thus a given wind direction will produce different wind-driven *SS* elevations at the two sites. Additionally, along-shore variations in SLPs will impart variations in *SS* due to the inverse barometer effect (IBE). The March 1983 event for which maxima were recorded at Los Angeles, for example, experienced SLPs below 99 kPa at Los Angeles and were consistently about 1 kPa higher at La Jolla. The difference in SLPs accounts for approximately 10 cm of the higher *SS* at Los Angeles as calculated by the inverse barometer effect, IBE = $\Delta P/(\rho g)$, where ΔP is the difference in atmospheric pressure (101.7 kPa – instantaneous pressure), ρ is saltwater density (= 1,025 kg/m^3), and g is the gravitational acceleration (9.81 m/s^2). Calculations of IBE for the entire available time-series shows that in cases where both winds and low SLPs contribute to positive surges, IBE accounts for ~50% of the total.

Though IBE is simple to calculate, the conditional dependency between wind-induced *SS* with shoreline orientation and wind duration, speed, and direction is not straight forward. Here we assume that nearshore *SWH*s implicitly represent wind speed, direction, duration and shoreline orientation through wave growth, propagation, and refraction across the shelf to the coast. Using the hindcast look-up-table-generated *SWH*s and SLPs from the CaRD10 database near the La Jolla tide gauge, a multi-linear regression model was developed,

$$SS = C_0 + C_1 \cdot \ln(SWH) + C_2[\Delta P/(\rho g)] \quad (2)$$

where the second term represents wind-induced *SS* and the last term represents changes in water levels due to IBE. To ensure the use of independent storms for development of the empirical storm surge model, events were first defined as those exceeding the 95th percentile (7.4 cm) and then 'declustered' by three days (Bromirski et al., 2003 (fig 7); Mendez et al., 2007; Ruggiero et al., 2010). Other exceedance levels were tested and found to yield similar results. The empirical coefficients were found to be C_0 =0.0474, C_1 = 0.0145 and C_2 = 1.2 via a least squares linear fit (R^2 = 0.15; RMSE = 0.06 m). Coefficients for the second term were fit using the *SS* time-series after removing the IBE. The low coefficient of determination is largely due to over-estimated setdown of ~5% of the data points in the observed range of 0 to -15 cm for which the model predicts -15 cm to -40 cm (not shown). Because affected data within this range is relatively small and because setdown is of less importance than setup in the context of this study where we seek extreme water levels conducive to flood hazards, we feel that these points do not significantly deter from the overall model fit. Although untested, it is expected that a wider continental shelf would produce higher C_1 and C_0 because of the limited rate of volumetric return flow.

Comparison of modeled SS to observed SS

SS measured at the La Jolla tide (LJ) gauge were used to develop the empirical storm surge model (Eq. 2), whereas *SS* measured at the Los Angeles (LA) tide gauge (9410660) were used to evaluate model skill. The choice of station data for model development (LJ) and model testing (LA) was arbitrary and found to make little difference with regard to the coefficients if the stations were switched. The range of the observation data are similar at La Jolla (used to develop the model) and Los Angeles (used to validate the model), however the distributions and histograms differ, particularly in that there are more frequent high events at the Los Angeles gauge and more frequent low events at the La Jolla gauge (fig. 4A). A hindcast time-series (1980-2014) for Los Angeles was calculated with Eq. (2), *SWH*s at nearshore point 2084 using the look-up-table, deep water observation data at CDIP067, and SLPs from CaRD10. A scatter plot of modeled and observed values indicate that the model does a reasonable job capturing the more frequent high events and fewer low events at the Los Angeles gauge, and that it replicates upper quantile *SS* levels above 0.25 m (fig. 4B; R^2 = 0.21; RMSE = 0.06 m).

Figure 4. Measured and modeled storm surge levels.

3.4 Empirical sea level anomaly model

Sea level anomalies are variations in water level forced by meteorological and oceanographic processes unrelated to storms (Theuerkauf et al., 2014). Elevated *SLA*s are often observed in conjunction with El Niño (Flick, 1998; Storlazzi and Griggs, 1998; Bromirski et al., 2003), which can yield water levels 10-20 cm above normal for several months (Cayan et al., 2008, 2009). Climate indices such as the North Atlantic Oscillation (NAO), Southern Oscillation Index (SOI), and Pacific-Decadal Oscillation (PDO) have been used to explain some of the variability in sea level (Mendez et al. 2007; Cayan et al. 2008; Serafin and Ruggiero 2014) and represent large-scale variability in the atmosphere and ocean over decadal and interdecadal time scales.

In an effort to maintain simplicity, correlations of *SLA*s with sea surface temperature anomalies (*SSTA*s) were developed from observations (1981 - 2014). Both observation and GCM *SSTA*s are readily available and are physically linked to *SLA*s directly through thermal expansion and indirectly through changes in large-scale wind patterns. *SSTA*s were computed by subtracting out the seasonal signal and long-term mean (1971-2000, Reynolds et al., 2002) from satellite-derived point-location *SST* time-series for 1981-2014 (NOAA/OAR/ESRL PSD). The resulting regression model has the form,

$$SLA = C_0 + C_1 \cdot \mathrm{SSTA} \qquad (3)$$

where the empirical coefficients C_0 and C_1 were found to equal 0.0546 and 0.0745, respectively, by a least squares linear fit through the upper envelope of the mean monthly *SSTA* and *SLA* measured at La Jolla (fig. 5; $R^2 = 0.83$). The upper envelope *SLA* was defined by the maximum *SLA* within 0.25° *SSTA* bins from -3.0°C to +3.0°C. A fit through the upper envelope, rather than all of the data, errs conservatively high by assuring a positive *SLA* for higher *SSTA*s. Due to scatter in the data and relatively small *SLA*s, a fit through all the data would yield only a slight positive *SLA* (~0.10 m) for the maximum observed *SSTA*, which is well below observed extremes.

Because of the coarse *SST* grid resolution (1° x 1°), La Jolla and Los Angeles are located at adjacent grid points with nearly identical *SST*s and thus evaluating model skill near Los Angeles with coefficients developed for La Jolla serves little purpose. The similarity between the two sites is supported with measured maximum mean monthly *SLAs*, which were only slightly higher at La Jolla (0.20 m) than at Los Angeles (0.18 m) and were both associated with the November 1997 El Niño.

Figure 5. Sea level anomalies.

3.5 Identification of offshore storm events and similarly responding coherent coastal segments

Coastal segments ('cells') that experience water level extrema of a specified return period in response to specific offshore storm conditions were defined by analyzing the projected TWL_{px} time-series at each cross-shore transect and grouping the corresponding offshore wave and wind conditions using cluster analyses. For example, to find regions that experience different absolute values of 20-year coastal storm-induced water levels (a total water level with a 1/20 = 5% chance of being exceeded in any one year) in response to different coastal storm conditions, four steps were taken. First, the 20-year recurrence TWL_{px}^{i} was calculated at each cross-shore transect. For simplicity, the 2012 through 2100 year projected time-series were complemented with TWL_{px} 11 years of data from 2012 to 2022 to generate full 100-year long time-series. The 3-hourly 100-year long time-series were de-clustered so that only peak events at least 3 days apart were analyzed. Using an r-largest value of 3 events per year (e.g., Coles 2001), the top 300 events at each cross-shore transect were sorted, ranked and assigned cumulative probabilities from which the relevant return period and levels were attained. Second, offshore wave (SWH, T_p, D_p) and wind forcing (U_a, U_{dir}) associated with each of the 20-year events at each cross-shore transect was identified. Wave and wind conditions were extracted from the same time-series that were used to generate the look-up-table-derived wave conditions, SLAs, and SS in the nearshore (Section 3). Lastly, the offshore wave and wind conditions associated with each of the cross-shore transects and the 20yr TWL_{px} were clustered using a *k*-means algorithm (Arthur and Vassailvitskii 2007). K-means treats each observation as an object having a location in parameter space and finds a partition in which objects within each cluster are as close to each other as possible, and as far as possible from objects in other clusters. Each cluster is defined by its member objects and their centroid which is the minimum sum of distances from all objects in that cluster. Here, clustering was performed with a 5-dimensional array of normalized offshore conditions, $X = [SWH^j, T_p^j, D_p^j, U_a^j, U_{dir}^j]$, where the superscript represents the j^{th} storm. Normalization was achieved by dividing each variable with the maximum corresponding time-series value so that each variable scaled between 0 and 1 and was equally weighted. Upon completion of the clustering, the centroids were dimensionalized by applying the opposite transformation of the normalization. Distances were calculated using the squared Euclidian form. Clustering was done 1,000 times, each with different randomly selected initial centroids using k-means++ seeding (Arthur and Vassilvitskii, 2007 cited in Mathworks® Matlab); the one with the lowest total sum of distances was saved in order to achieve robust representations of groupings and centroid locations. Following the described approach, offshore storm conditions and coastal cells were grouped for the 1-yr, 20-yr, and 100-yr TWL_{px} return periods.

4 Results

Winds, sea level pressures, and sea surface temperatures from GFDL-ESM2M under the RCP 4.5 climate scenario served as boundary conditions to the models outlined in the previous section and were used to generate continuous historical and projected time-series of $R_{2\%}$, SS, SLA, and TWL_{px} at each of the cross-shore transects within the Southern California Bight. Each of these components are discussed in the following sub-sections.

4.1 Wave runup

For computation of $R_{2\%}$ (Eq. 1), wave heights and peak periods were downscaled to the local level using the look-up-table and times-series of offshore wind and deep-water wave conditions at CDIP067 (Section 3.1). Bight-wide averaged historical $R_{2\%}$ levels are 0.64 m with a maximum of 1.97 m, assuming a representative foreshore slope of β_f = 0.03 (fig. 6A). Three 30-year future time periods are compared to the historical climatology: start (2012-2040), middle (2041-2070), and end (2071-2100) of the 21st century. Bight-wide averaged $R_{2\%}$ during each of the projected time periods are nearly identical to the historical time period (0.65 m). Time-period maxima are projected to be highest during the mid-part of the century with a bight-wide average 15% increase (2.22 m versus 1.97 m).

Figure 6. Bight-wide averaged time-series of historical and projected coastal water levels using downscaled GFDL-ESM2M, RCP4.5.

Changes in extreme $R_{2\%}$, calculated as the percent change of the 98th percentile exceedances at each cross-shore transect between the future and historical time periods, are evaluated spatially and temporally in figure 7. Results indicate an overall increase of 1.2% (range from -1.0% to 3.1%) in 98th percentile $R_{2\%}$ during the start of the 21st century and overall little change (-0.1%) during the mid-part of the century followed by greater decreases (-1.7%) by the end of the century. The largest increases are projected for the Los Angeles/Long Beach coast where 98th percentile $R_{2\%}$ is projected to increase by as much as 4.5% and 4.3% for the mid- and end-century time-periods, respectively. Greatest decreases in extreme $R_{2\%}$ are projected for mid San Diego, mid Los Angeles, and parts of Santa Barbara counties. San Diego exhibits the largest decreases approaching -4.5%. The decrease is primarily related to projected decreases in extreme *SWH*s and with D_p from more southerly directions.

Figure 7. Percent change of extremes between three 30-year projected time-slices and the historical time-period (1976 – 2005).

4.2 Storm surge

Storm surges (Eq. 2) were estimated with the same time-series of *SWH*s as used for calculation of $R_{2\%}$, and SLP time-series extracted from the GCM ocean grid point closest to the study area. SLPs from this single grid point were used to estimate the IBE component of the total storm surge signal, calculated as the deviation from the average historical (1976-2005) SLP (101.83kPa). Because a single SLP time-series was used, the IBE contribution was spatially-uniform across the Bight, in contrast to the wind-induced component of the total storm surge which varies with alongshore variations in *SWH*s. 6-hourly GCM SLPs were linearly interpolated to the 3-hour time intervals of the *SWH* time-series prior to computing the total *SS*.

Bight-wide averaged historical *SS* range from -0.26 m to +0.34 m. The projected time-series exhibit similar ranges from -0.24 m to +0.35 m with no apparent trend (fig. 6B). Extreme (98th percentile) *SS* at individual cross-shore transects are projected to decrease by approximately -3.2%, -1.6%, and -6.8% during the start, middle, and end of the 21st century as compared to the historical time period (fig. 7B).

4.3 Sea level anomalies

*SLA*s were first calculated on a monthly time scale, as the model is based on monthly anomalies of SSTs (Eq. 3), and then linearly interpolated to the same 3-hour time intervals as *SS* and $R_{2\%}$. Four distinct regions of identical *SLA* variations were computed from SST time-series at four grid points within the Bight on the GCM ocean grid; anomalies were calculated relative to the long-term mean of each of the three future time-periods. The four regions are segmented into cross-shore transects 1 to 1360, 1361 to 2593, 2594 to 3720, and 3721 to 4802 (fig. 7C).

Mean monthly historical SSTs range from 15.2°C in January to 25.3°C in September and are on average 1.4 °C (range 0.3°C to 2.5°C) warmer in the south compared to the north part of the Bight (fig. 8). Mean monthly SSTs are projected to be 0.7°C warmer by the end of the 21st century averaged over all months (range 0.3°C to 1.1°C). SSTs are projected to increase most dramatically during the summer months. For example, September monthly means from 2012 to 2100 exhibit a linear increase of 0.02 °C / yr (r = 0.49; p-value < 0.005). The linear increase is also reflected in projected *SLA*s since the empirical model in Eq. (3) is a linear function of SST anomalies (fig. 6C). Extreme (98th percentile) *SLA*s are projected to reach 0.22 m to 0.24 m by the mid and end of the century, compared to 0.16 m to 0.18 m during the historical time-period and the start of the 21st century (2012-2040) reflecting increases >30% (fig. 7C). Previous studies have shown that SST trends of the GFDL-ESM2M are commensurate with other GCMs (e.g., Zhang et al, 2014), and thus, while mean monthly SSTs within the Southern California Bight from other GCMs were not specifically calculated for this study, the noted trends are likely representative of projected conditions.

Figure 8. GCM modeled monthly mean SSTs within the Southern California Bight.

4.4 *TWL* proxies

TWL_{px} were calculated at 4,802 discrete points along the 10 m isobath within the Southern California Bight from the linear summation of $R_{2\%}$, *SS*, and *SLA* (fig. 7D). The relative percent change in extreme TWL_{px} is similar to $R_{2\%}$ for the first part of the century (~2% increase), but by the middle and end of the century, *SS* and *SLA* play a larger role in the change signal. The greatest relative change is projected to occur during the mid-part of the century when extreme TWL_{px} are estimated to be >5% greater at some locales. Increases are projected to be less pronounced at the southern and northern ends of the Bight, largely due to the lower projected $R_{2\%}$ along those coastal stretches (fig. 7A).

4.5 Storm events and similarly responding coherent coastal segments

Clustering of the offshore wave and wind conditions with the corresponding locally derived 1-year, 20-year, and 100-year return period TWL_{px} extremes shows that a number of different storms of varying intensity and direction are responsible for the annual and 20-year events, whereas the coastal response is more spatially uniform if considering the 100-yr event (fig. 9, Table 4). That is, along most sections of the Southern California Bight, the local impacts of a 100-yr coastal event are likely to occur from the same offshore storm (red hued colors in fig. 9, Table 4C), but the less severe 1-yr local coastal flood event is likely to occur from many different storms (green hued colors in dig. 10, Table 4A). Annual exceedance levels for more than 70% of the Bight (computed as the number of cross-shore transects that fall within a given grouping or storm divided by the total number of cross-shore transects, last columns in Table 4) is represented by 5 storms, whereas nearly 80% of the region is represented by 4 storms for the less frequent but higher intensity 20 yr RP. For the 100-yr RP, a single storm, with a clustered centroid at SWH= 7.04 m, T_p = 19s, D_p = 283°, U_a = 7.1 m/s, and U_{dir} = 308° captures 95% of the region. Thus, the return period threshold that delivers near uniform response intensities is somewhere between the 20-yr and 100-yr return period.

Figure 9. Coastal cells that respond similarly to coastal storms.

The weighted means of SWH, T_p, and U_a (calculated as $\bar{x} = (\sum_{i=1}^{N} w_i x_i)/\sum_{i=1}^{N} w_i$, where x is the variable in question, w is the percent area affected, the subscript i is the storm number, and N is the total number of storms) suggest that seas and winds are relatively more important with regards to the TWL_{px} for less severe but more frequent storms compared to the higher intensity coastal storms. This is evidenced by the stronger wind speeds (8.1 m/s < $\overline{U_a}$ < 8.3 m/s) of the 1-yr and 20-yr return periods compared to the 100-yr return period winds (7.3 m/s) and that conversely, $\overline{SWH}$ and $\overline{T_p}$ increase with increasing storm severity, from 4.44 m to 7.00 m and from 15 s to 19 s for the 1-yr and 100-yr RPs, respectively. Additionally, the northwesterly along-coast winds of the 100-yr return period are shadowed with regards to local wave generation compared to the southwesterly winds (367°-350°) of the 1-yr and 20-yr return periods which are directed onshore (arrows in fig. 9). Exceptions to this exist, particularly along the west-facing coast of San Diego and extreme northern part of the study area near Point Conception.

Table 4A. Projected offshore wave and wind conditions that result in 1-yr return period (RP) coastal storm events along the coast of the Southern California Bight.

RP 1 yr Event	***SWH* (m)**	**T_p (s)**	**D_p (deg)**	**U_a (m/s)**	**U_{dir} (deg)**	**Area affected**	**colors in fig. 9**
Storm 1	3.92	16	286	5.7	312	16%	
Storm 2	4.15	16	289	5.0	58	15%	
Storm 3	5.31	15	293	11.4	294	14%	
Storm 4	4.42	13	279	11.1	230	13%	
Storm 5	5.08	16	293	7.3	334	13%	
Storm 6	4.87	16	290	5.9	228	12%	
Storm 7	3.40	13	286	10.2	312	9%	
Storm 8	4.66	13	288	16.2	304	5%	
Storm 9	2.90	14	262	4.0	211	2%	
Range	3.40 to 5.31	13 to 16	279 to 293	5.0 to 16.2	58 to 334		
Wtd. mean	4.44	15	287	8.3	250		

Table 4B. Same as previous but for 20-yr RP.

RP 20 yr Event	***SWH* (m)**	**T_p (s)**	**D_p (deg)**	**U_a (m/s)**	**U_{dir} (deg)**	**Area affected**	**colors in fig. 9**
Storm 1	6.24	18	288	7.8	274	30%	
Storm 2	6.42	18	301	12.2	335	22%	
Storm 3	6.32	16	279	4.9	89	14%	
Storm 4	5.85	18	281	5.7	166	12%	
Storm 5	6.08	18	289	5.9	211	10%	
Storm 6	3.74	14	291	11.6	310	6%	
Storm 7	6.96	16	277	9.4	151	4%	
Storm 8	2.90	16	284	2.8	229	3%	
Storm 9	4.32	17	288	10.8	143	1%	
Range	2.90 to 6.96	14 to 18	277 to 301	2.8 to 12.2	89 to 335		
Wtd. mean	6.00	17	289	8.1	237		

Table 4C. Same as previous but for 100-yr RP.

RP 100 yr Event	***SWH* (m)**	**T_p (s)**	**D_p (deg)**	**U_a (m/s)**	**U_{dir} (deg)**	**Area affected**	**colors in fig. 9**
Storm 1	7.04	19	283	7.1	308	95%	
Storm 2	6.96	16	277	9.4	151	3%	
Storm 3	5.64	20	295	12.7	344	2%	
Storm 4	5.90	17	281	6.8	319	<1%	
Storm 5	5.86	18	281	5.7	166	<1%	
Storm 6	6.09	18	290	5.9	209	<1%	
Storm 7	6.83	17	306	12.5	323	<1%	
Storm 8	-	-	-	-	-	0%	
Storm 9	-	-	-	-	-	0%	
Range	5.64 to 7.04	16 to 20	277 to 306	5.7 to 12.7	151 to 344		
Wtd. mean	7.00	19	283	7.3	304		

A total of 9 mutually exclusive clusters were initially used to identify the coherent coastal sections. This number of clusters was settled upon after incrementally reducing the number of clusters such that no single cluster represented less than 2% of the coastal area affected for the 1-year return period events, the storm-case with the highest degree of variability. However, for detailed computationally costly numerical modeling it is often necessary to further reduce the number of relevant events so that overall computation time is manageable yet ensuring coastal hazard vulnerability is adequately captured. To this end, we used a combination of 1) the result that fewer storms are required for representation of higher intensity storms (see previous paragraphs), 2) evaluation of the range in offshore forcing variables (e.g.,~10° variation in D_p of most prominent 1-yr and 20yr return period storms), and 3) the Silhouette graphical aid of Rousseuw (1987) which allows for assessment and selection of group exclusivity. The combination of these three considerations resulted in re-grouping the 1-yr and 20-yr return period storms into 3 and 2 groups, respectively. Re-grouping of the 100-yr return period was not done since 95% of the area is represented with one single event (Table 4C).

Storm dates for the 1-yr and 20-yr return periods were identified by performing a Quickhull best match search (Barber et al. 1996) of the storm group centroids with the 100-year long time-series of the 5 parameters ($X = [SWH^t, T_p^t, D_p^t, U_a^t, U_{dir}^t]$, where *t* is the time-step). Maximum SWH and U_a within ±12 hours of the identified storm date were then extracted in addition to T_p, D_p and U_{dir} associated with those maxima. All 5 storm dates (3 for the 1-yr and 2 for the 20-yr RP) are between the months of December through March, as is expected for intense storm activity in the study area (Table 5). Resultant SWHs range from 4.19 m to 4.90 m and from 5.86 m to 6.13 m for the 1-yr and 20-yr RPs, respectively, commensurate with the weighted means of the 9-member storm grouping (Table 4). T_p and D_p behave similarly ranging from 13 s for the 1-yr return period to 18 s for the 20-yr return period and with wave incidence angles from west-northwest (281° to 292°). Winds range from 5.7 m/s to 11.5 m/s, with one wind direction emanating from the northwest and one from the southwest. The northwesterly winds (322°) of the 20-year event are associated with the higher SWH (6.13 m) of the two storms. In contrast, higher SWH during the 1-year event are linked to onshore winds from the southwest quadrant, again indicating the increased importance of local seas on TWL_{px} for the more frequent but less intense storms.

Table 5. Storm dates and offshore conditions for which the GFDL-ESM2M RCP4.5 model captures local annual and 20-yr return period storms in the Southern California Bight.

Storm dates		***SWH* (m)**	**T_p (s)**	**D_p (deg)**	**U_a (m/s)**	**U_{dir} (deg)**	**Area affected**
RP 1 yr	Mar 2020	4.39	16	284	7.5	284	42%
	Dec 2056	4.90	13	292	11.5	242	39%
	Jan 2097	4.19	17	292	5.7	82	19%
RP	Feb 2095	6.13	18	292	11.1	322	58%

	Feb 2025	5.86	18	281	7.1	177	42%

To test the sensitivity of the storm selection process and identification of coherent coastal cells on availability of foreshore slope data, which is often not available across large stretches of coast, the same scripts were applied to TWLpx consisting of runup elevations calculated using transect-specific foreshore slopes (as used in the runup equation). Clustering the data into 9 mutually exclusive clusters yields identical results to those in Table 9C for the 100-yr storm using a region-wide averaged slope at all transects. For the 1-yr and 20-yr return period storms, the overall bulk statistics (range and averages) are very similar for the two cases; a mean difference of ΔSWH = 14 cm, ΔT_p = 0 s, and $\Delta D_p = 3°$ for the 1-year event and a difference of ΔSWH = 11 cm, ΔT_p = 0 s, and $\Delta D_p = 1°$ degrees for the 20-year event. The differences are greatest for the 1-year return period storms across ~20% of the region where differences in SWH and D_p are as much as 60 cm and 20°.

Reducing the number of storm clusters to 3 and 2 for the 1-year and 2-year storm events, respectively, the difference between the two cases reduces to a maximum absolute SWH bias of 30 cm and 14 cm for the 1-year and 20-year return periods. The difference in T_p and D_p are < 1 s and <4°, respectively and the area distributions are about the same (differences in the spatial maps are difficult to distinguish and thus is not shown). Thus, the use of a varying slope does slightly change the identification of offshore storm conditions, particularly for the less severe annual return period storm. But the areas affected are small (<20%) and the differences reduce when the number of storms are restricted.

5 Discussion

Employing the GFDL-ESM2M RCP 4.5 climate scenario, extreme TWL_{px} are projected to be at their highest levels within the Southern California Bight during the middle of the 21st century (fig. 7D). Higher TWL_{px} are also projected for early in the century, but by the end of the century, TWL_{px} are only marginally greater compared to the recent past. Increases in mean $R_{2\%}$ are primarily attributed to increasing average T_p. The projected increase and decrease of T_p and SWH, respectively, are consistent with previous studies which have found similar trends in deep water locales offshore of Southern California using other GCM winds and global (Hemer et al., 2013) or regional (Graham et al., 2012) scale wave simulations. Graham et al. (2012) attributed decreasing SWH to reductions in wind speed along the southern flank of the main core of the westerlies. Increasing T_p is thought to be a result of increasing wave energy in the southern hemisphere (Semedo et al. 2013; Erikson et al. 2015).

$R_{2\%}$ accounts for more than 85% of the extreme TWL_{px} making it the largest contributor to storm generated flooding along this high energy open coast (Table 6). SLA accounts for nearly 10% of the TWL_{px} signal with the remainder (~3.5%) attributable to SS. $R_{2\%}$ is however quite sensitive to the foreshore slope and thus its relative contribution compared to SS and SLA varies. Under identical conditions but with prevailing steeper foreshore slopes, of for example $\beta_f = 0.15$,

$R_{2\%}$ contributions account for all but 3% to 4% of the extreme TWL_{px}. The same computation using real-valued foreshore slopes for each cross-shore transect ('varying β_f' in Table 6) and then averaging across all sites yields results similar to using the regionally averaged slope.

For identification of individual storm events and affected coastal sections, use of real-valued foreshore slopes as opposed to the region-wide average, has no effect on the more extreme 100-yr event but identifies different storms for ~20% of the area when seeking identification of 1-yr storm events. However, the site-specific foreshore slopes used here were extracted from elevation models compiled from single time-points, and because slopes vary seasonally and inter-annually, these site-specific foreshore slopes might not be the best proxy for when annual storms occur. Thus, for most accurate results of lower intensity (e.g., 1-year return period) storms, foreshore slopes that are representative of conditions prior to such events would be most useful but often very difficult to obtain and thus a regional average might still be the best option.

The fact that $R_{2\%}$ dominates the TWL_{px} signal and hence the flood potential, a result consistent with the recent findings of Serafin et al. (2017), highlights the importance for accurate representations of the wave climate and dynamic changes in coastal bathymetry. Though the wave climate is dynamically downscaled to the local level, changes in wave growth, refraction, shoaling and subsequent wave heights due to increasing water depths from sea level rise, storm surge, and other sea level anomalies are not accounted for in the calculations of SWH and T_p, which were extracted at the 10 m isobath and used to calculate runup for the TWL_{px}. Such effects could be included by generating separate wave transformation look-up-tables (Section 3.1) using a set of pre-determined sea level rise scenarios commensurate with the projected SLR curve of the GCM used in the study and discrete rises in water levels to account for SS and SLA. However, because runup is the dominant variable, accounting for >85% of the TWL_{px} in this region, any reduction of this parameter would likely still dominate the storm selection and identification of coherent coastal sections. Moreover, with an increase in SLR, *SWH*s and consequently runup will mostly increase due to the greater depth and distance over which wave growth can occur, further increasing the relative importance of SWH on the storm identification results.

Table 6. Percent contributions of individual components to extreme TWL_{px}.
[computed from hourly time-series spanning 2012 – 2100 and exceeding the 98th percentile TWL_{px}]

	Foreshore slope		
	$\beta_f = 0.03$	$\beta_f = 0.15$	*varying* β_f
$R_{2\%}$	86.6 ± 0.9	96.7 ± 0.4	90.4±1.9
SS	3.5 ± 0.4	1.1 ± 0.2	3.7±0.5
SLA	9.9 ± 0.5	2.2 ± 0.3	5.9±1.4

For the GCM and climate change scenario examined here (GFDL-ESM2M, RCP4.5), extreme (98th percentile) *SS* are projected to decrease; most of the decrease is attributable to inverse barometer effects resulting from changes in low SLPs. Using observation data, Cayan et al. (2008) showed that the greatest influence on short period non-tidal sea level variability in La Jolla was due to IBEs and commensurate with the findings of this study. The frequency of occurrence of extreme low SLPs, computed as those levels that dip below the 2% historical low of 100.795kPa, are projected to decrease from occurring 1% of the time during the historical time-period to 0.7% of the time by the end of the century. While uncertain, this may be a reflection of an apparent poleward shift of low pressure system storm tracks (Yin, 2005; Hu and Fu, 2007), a trend which appears to have been amplified during recent El Niño events (Barnard et al., 2017).

SLAs are found to contribute approximately 10% to the extreme TWL_{px} using the linear relationship developed for this study. The 'SLA model' is based on a simple linear but strong (R^2 = 0.83) relationship between local SST anomalies and upper envelope SLAs. It is noted that the relatively greater contribution of SLA to the TWL_{px} compared to SS might well be because the upper SLA envelope was used to develop the empirical model, whereas a more conservative model was developed for SS.

Winter storms, extreme waves, flooding, significant coastal erosion, and elevated SLAs in Southern California are strongly linked to El Niño events (Dettinger et al. 2001; Barnard et al., 2015). El Niño generation and teleconnections are simulated in GCMs (Bellenger et al., 2014; Mentashi et al., 2017) and while SST anomalies are generally indicative of El Niño events (Lau and Nath, 1996), the linear model would likely benefit from further developments, through for example, the use of additional variables, inclusion of climate indices, and/or perhaps applications of neural networks or genetic algorithms.

Via an iterative process it was found that at least 25 (= 9 + 9 + 7, per Table 4) separate storm events are responsible for the 1-yr, 20-yr, and 100-yr return period TWL_{px} along the shores of the Southern California Bight. A desire for comprehensiveness stipulates that detailed deterministic modeling of all the events should be conducted to fully represent all storm levels and locales, however this is not always feasible and a smaller number of representative storms are often desired. To this end, the number of clusters was reduced to 3, 2, and 1 for the 1-yr, 20-yr, and 100-yr events, respectively, and associated storm dates that capture these return level responses across larger coastal cells were determined. This reduced the computation time nearly four-fold (from 25 to 6 full detailed runs). This approach allows for robust identification of group response considering limitations put forth by the needs of the study (in this case a need to reduce the number of events for subsequent deterministic full numerical modeling), but with the recognition that specific return period events might be better represented by slightly different storms. For situations such as the one presented here, particular care was needed to ensure that incident wave directions from the reduced number of clusters adequately represented D_p in the full list of 9 storms.

6 Conclusions

A computationally efficient method and accompanying models are developed to identify GCM-driven storm events that result in coastal flood hazards along coherent sections of a shoreline subjected to spatially-varying winds, wave patterns, storm surge, and other non-tidal water level fluctuations. Coherent coastal cells are found by *k*-means clustering of TWL_{px} extremes computed at closely spaced intervals (~100 m) along the shore. Storm dates of select local return period events are found by relating the coastal cell responses to region-wide storms characterized by offshore GCM wind and wave conditions. The method and models are developed and implemented using outputs from the GFDL-ESM2M RCP4.5 climate change scenario downscaled to the Southern California Bight, an area punctuated by islands, canyons, and varying shoreline orientations.

Clustering of 1-yr, 20-yr, and 100-yr return period local TWL_{px} show that the more severe but rare coastal flood events (e.g., the 100-yr event) typically occur from the same storm, and that a number of different storms are responsible for the less severe but more frequent local extreme water levels. For Southern California, the return period threshold that delivers near uniform response intensities along the coast is between the 20-yr and 100-yr events. Identification of the storm dates and analysis of the associated region-wide GCM wind and wave conditions indicates that distantly generated swell are relatively more important than locally generated waves for the more intense 100-yr storm compared to the 1-yr and 20-yr return period events.

In the absence of tides, results show that extreme TWL_{px}, defined as the 98th percentile of each 100-year long time-series at each nearshore point, are dominated by $R_{2\%}$ (>85%) along this high-energy open coast. The joint occurrence of tides and high wave events was not evaluated in this study since the focus was on identifying storm events from large scale GCMs that are not temporally accurate to the hour (in contrast to deterministically computed astronomic tides). It is recognized however, that in areas with meso- to macro-scale tides, nearshore wave heights, runup, and storm surge are influenced by tide-related depth changes and currents. In this study, these nonlinear effects are assumed to be small enough to not significantly affect the storm selection process.

The fact that $R_{2\%}$ dominates the non-tidal TWL_{px} signal highlights the importance for accurate representation of the wave climate along this complex coastline. Prior to calculating $R_{2\%}$, waves were propagated to the nearshore with the use of a look-up-table developed from hindcasted numerical wave simulations. Spatial patterns generated with the numerical wave model clearly show lower *SWH*s along sections of the coast where $R_{2\%}$ might otherwise be over-estimated if changes in wave energy and direction due to island shadowing and complex geography and bathymetry were not accounted for.

Comparison of projected and historical extreme TWL_{px} indicate that the greatest relative change, assuming the RCP4.5 climate scenario and GFDL-ESM2M, will occur during the middle of the century. Extreme TWL_{px}, are estimated to be approximately 3% greater during 2041-2070 compared to the 1976-2005 historical time period. By the end of the century, $R_{2\%}$ is projected to decrease in response to lower extreme *SWH*, resulting in TWL_{px} that are only marginally greater than historical extremes. Along sheltered regions of the coast where $R_{2\%}$ are small, *SLA* dominates the TWL_{px} signal resulting in a near 4% increase of extreme TWL_{px} at the end of the century. Extreme *SLA*, primarily associated with El Niño effects, were modeled with a simple but conservatively high linear regression model that relates observed sea-surface temperature anomalies to the upper-envelope of *SLA*s measured at a tide gauge within the study area.

The storm dates and affected coastal cells identified as part of this study have been used to simulate locally derived return period storms in combination with various sea level states using the deterministic CoSMoS model (e.g, Barnard et al. 2014). Future work may include comparing the CoSMoS model results to TWL_{px} to evaluate whether or not the added computation time and effort of the deterministic model provides much improved flood levels compared to the quicker superposition of components to estimate *TWL*s.

Acknowledgements

This work was funded by the U.S. Geological Survey (USGS) Coastal and Marine Geology Program, California State Coastal Conservancy, California Department of Fish and Wildlife, and the Tijuana River National Estuarine Research Reserve and carried out under the USGS project **'**Determining the risk of flooding and erosion hazards due to climate change for the Southern California coast'. PR and KS also received support from the NOAA Coastal and Ocean Climate Applications (COCA) program (NA15OAR4310243). Data is available for download at https://walrus.wr.usgs.gov/coastal_processes/cosmos/socal3.0/. We acknowledge and thank NCEP and Scripps Institution of Oceanography, particularly Dr. Dan Cayan, Dr. David Pierce, and Mary Tyree, for producing and making available their global and local wind and sea level pressure model outputs. The insightful reviews by Sean Crosby and two anonymous journal reviewers significantly improved the manuscript and are greatly appreciated. Any use of trade, firm, or product names is for descriptive purposes only and does not imply endorsement by the U.S. Government.

References

Adams, P.N., Inman, D.L., and Graham, N.E., 2008. Southern California Deep-Water Wave Climate: Characterization and Application to Coastal Processes. Journal of Coastal Research: 24(4), 1022 – 1035.

Allan, J.C., Ruggiero, P., and Roberts, J. T., 2012. Coastal Flood Insurance Study, Coos County, Oregon, Oregon Department of Geology and Mineral Industries Special Paper 44, 119 pp.

Arthur, D., Vassilvitskii. S., 2007. K-means++: The Advantages of Careful Seeding." SODA '07: Proc. Eighteenth Annual ACM-SIAM Symposium on Discrete Algorithms, 1027–1035.

Barber, C. B., D.P. Dobkin, and H.T. Huhdanpaa, 1996. The Quickhull Algorithm for Convex Hulls, ACM Trans. Math. Software, 22, 4, 469-483.
Barnard, P.L., Hoover, D.J., Hubbard, D.M., Snyder, A., Ludka, B.C., Allan, J., Kaminsky, G.M., Ruggiero, P., Gallien, T.W., Gabel, L., McCandless, D., Weiner, H.M., Cohn, N., Anderson, D.L. and Serafin, K.A., 2017. Extreme oceanographic forcing and coastal response due to the 2015-2016 El Niño. Nat. Comm., 8 (14365), 8 pp.
Barnard, P.L., Short, A.D., Harley, M.D., Splinter, K.D., Vitousek, S., Turner, I.L., Allan, J., Banno, M., Bryan, K.R., Doria, A., Hansen, J.E., Kato, S., Kuriyama, Y., Randall-Goodwin, E., Ruggiero, P., Walker, I.J. and Heathfield, D.K., 2015. Coastal vulnerability across the Pacific dominated by El Niño/Southern Oscillation. Nat. Geos., 8 (801-807).
Barnard, P.L., van Ormondt, M., Erikson, L.H., Eshleman, J., Hapke, C., Ruggiero, P., Adams, P.N. and Foxgrover, A.C., 2014. Development of the Coastal Storm Modeling System (CoSMoS) for predicting the impact of storms on high-energy, active-margin coasts. Natural Hazards, Volume 74 (2), p. 1095-1125, http://dx.doi.org/10.1007/s11069-014-1236-y
Battjes, J., and Janssen, J., 1978. Energy loss and set-up due to breaking of random waves. In Proceedings 16th International Conference Coastal Engineering, ASCE, 569-587.
Bellenger, H., Guilyardi, E., Leloup, J., Lengaigne, and M., Vialard, J., 2014. ENSO representation in climate models: from CMIP3 and CMIP5. Climate Dynamics, 42, 7-8.
Booij, N., Ris, R.C., and Holthuijsen, L.H., 1999. A third generation model for coastal regions, Part I – Model description and validation. Journal of Geophysical Research, 104(C4), 7649-7666.
Bromirski, P.D., Flick, R.E., and Cayan, D.R., 2003. Storminess variability along the California coast: 1858–2000, Journal of Climate, 16(6), 982–993.
Callaghan, D. P., Nielsen, P., Short, A., and Ranasinghe, R, 2008. Statistical simulation of wave climate and extreme beach erosion. Coastal Eng., 55, 5 375-390.
Camus, P., M. Menendez, Mendez, F. J., Izaguirre, C., Espejo, A., Canovas, V., Perez, J., Rueda, A., Losada, I. J., and Medina, R., 2014. A weather-type statistical downscaling framework for ocean wave climate, J. Geophys. Res. Oceans, 119.
Cayan, D.R., Bromirski, P.D., Hayhoe, K., Tyree, M., Dettinger, M.D., Flick, R.E., 2008. Climate change projections of sea level extremes along the California coast. Climate Change, S57-S73.
Cayan, D.R., Tyree, M., Dettinger, M., Hidalgo, H.., Das, T., Maurer, E., Bormirski, P., Graham, N., and Flick, R., 2009. Climate change scenarios and sea level rise estimates for the California 2009 climate change scenario assessment. California Climate Change Center, CEC-500-2009-014-F. 64pp.
Chawla, A., Spindler, D.M., Tolman, H.L., 2013. Validation of a thirty year wave hindcast using the Climate Forecast System Reanalysis winds. Ocean Modelling,70, 189-206.
Christiansen R.L., Yeats, R.S., 1992. Post-Laramide geology of the U.S. Cordilleran region. In: Burchfiel BC, Lipman PW, and Zoback ML (eds), The Cordilleran Region: conterminous U.S.: the geology of North America [DNAG] Vol. G-3: Geol. Soc. America, 261–406.
CIRIA, CUR, and CEFMEF, 2007. Physical site conditions and data collection. In The Rock Manual, C683.
Coastal Data Information Program (CDIP), 2017. Scripps Institution of Oceanography, San Diego. Integrative Oceanography Division. http://cdip.ucsd.edu.
Coles, S. 2001. An Introduction to Statistical Modeling of Etreme Values. Springer.

Crosby, S.C., O'Reilly, W.C., and Guza, R.T., 2016. Modeling long period swell in southern California: practical boundary conditions from buoy observations and global wave model predictions. J. Atm. Ocean Technology, 33, 16673-1690.

Danielson, J.J., Poppenga, S.K., Brock, J.C., Evans, G.A., Tyler, D.J., Gesch, D.B., Thatcher, C.A., and Barras, J.A., 2016, Topobathymetric elevation model development using a new methodology—Coastal National Elevation Database: Journal of Coastal Research, SI no. 76, p. 75–89, doi: 10.2112/SI76-008

Dettinger, M.D., Battisti, D.S., Garreaud, R.D., McCabe, G.J., and Bitz, C.M., 2001, Interhemispheric effects of interannual and decadal ENSO-like climate variations on the Americas, In Present and Past Interhemispheric Climate Linkages in the Americas and Their Societal Effects.Academic Press, 1-16.

Egbert, G., Bennet, A., Foreman, M., 1994. TOPEX/POSEIDON tides estimated using a global inverse model. Journal of Geophysical Research 99 (C12), 821–824.

Erikson, L.H., Barnard, P.L., Eshleman, J., Foxgrover, A., O'Neill, A., Fitzgibbon, M., and Ballard, G., in review. A coastal storm modeling system for determination of flood hazards along a high energy coast in response to sea level rise and 21st century storms: CoSMoS in the San Francisco region.

Erikson, L.H., Hegermiller, C.A., Barnard, P.L., Ruggiero, P., and van Ormondt, M., 2015. Projected wave conditions in the Eastern North Pacific under the influence of two CMIP5 climate scenarios. Ocean Modelling, Special Issue: Ocean Surface Waves, 96(1), 171-185.

Erikson, L.H., Hanes, D. M., Barnard, P. L., and Gibbs, A. E., 2007. Swash zone characteristics at Ocean Beach, CA. Proc. Int. Conf. Coastal Eng., 909-921.

Flick, R. E., 1998. Comparison of California tides, storm surges, and mean sea level during the El Niño winters of 1982–1983 and 1997–1998. Shore & Beach 66(3):7–11.

Graham, N. and Diaz, H., 2001. Evidence for Intensification of North Pacific Winter Cyclones since 1948. Bull. Amer. Met. Soc. 82,1869-1893.

Graham, N., Cayan, D.R., Bromirski, P.D., Flick, R.E., 2012. Multi-model projections of twenty-first century North Pacific winter wave climate under the IPCC A2 scenario. Climate Dynamics, Springer, 26 pp. DOI 10.1007/s00382-012-1435-8

Haigh, I. D., Wijeratne, E., MacPherson, L. R., Pattiaratchi, C. B., Mason, M. S., Crompton, P. P., and George, S., 2013, Estimating present day extreme water level exceedance probabilities around the coastline of Australia: Tides, extra-tropical storm surges and mean sea level, Clim. Dyn., 42(1–2), 121–138.

Harper, B., T., Hardy, L., Mason and Fryar, R., 2009. Developments in stormtide modelling and risk assessment in the Australian region. Natural Hazards. 51(1), 225-238.

Hasselmann, K., Barnett, T.P., Bouws, E., Carlson, H., Cartwright, D.E., Enke, K., Ewing, J.A., Gienapp, H. · Hasselmann, D.E. ·Kruseman, P. · Meerburg, A. · Müller, P. · Olbers, D.J. , Richter, K., Sell, W., and Walden, H., 1973. Measurements of wind-wave growth and swell decay during the Joint North Sea Wave Project (JONSWAP). Deutches Hydrographisches Institut, 93 pp.

Hegermiller, C.A., Rueda, A., Erikson, L.H., Barnard, P.L., Antolinez, J.A.A., Mendez, F.J., 2017. Controls of multimodal wave conditions in a complex coastal setting, Geoph. Res. Lttrs.

Hegermiller, C.E., Erikson, L.H., and Barnard, P.L., 2016. Nearshore waves in the Southern California Bight: A 30-year hindcast and 90-year projected time-series for the 21st century. U.S. Geological Survey summary of methods to accompany data release.

Hemer, M. A., Y. Fan, N. Mori, A. Semedo, and X. L. Wang, 2013. Projected changes in wave climate from a multi-model ensemble. Nature Climate Change, 3, 471-476.

Hibbard, K.A., Meehl, G.A., Cox, P.M., Friedlingstein, P., 2007. A strategy for climate change stabilization experimetns. EOS Trans. Am. Geophys. Union, 88, 217-221.

Hoeke, R.K., McInnes, K.L., Kruger, J., McNaught, R., Hunter, J., and Smithers, S., 2013. Widespread inundation of Pacific islands by distant-source wind-waves. Global and Planetary Change, 108, 128-138.

Hogarth L., Babcock J., Driscoll N., Dantec N., Haas J., Inman D., and Masters P., 2007. Long-term tectonic control on Holocene shelf sedimentation offshore La Jolla, California. Geology 35(3):275.

Horsburgh, K. L. & Wilson, C. Tide–surge interaction and its role in the distribution of surge residuals in the North Sea. J. Geophy. Res. 112, CO8003 (2007).

Hu, Y. and Fu, Q., 2007. Observed poleward expansion of the Hadley circulation since 1979. Atmos. Chem. Phys. 7, 5229–5236.

Hunt, I.A., 1959. Design of seawalls and breakwaters. J. of Waterways and Harbours Division, ASCE 85, (WW3), 123–152.

Kanamaru H., and Kanamitsu, M., 2007. Fifty-seven-year California reanalysis downscaling at 10 km (card10). Part ii: comparison with North American regional reanalysis. J. Climate, 20, 5572–5592.

Komen, G.J, Cavaleri, L., Donelan, M., Hasselmann, K., Hasselmann, S. and Janssen, P.A.E.M., 1994. Dynamics and Modeling of Ocean Waves. Cambridge University Press, 532 pp.

Lau, N-G, and Nath, M. J., 1996. The role of the atmospheric bridge in linking tropical Pacific ENSO events to extratropical SST anomalies. J. Climate, 9, 2036-2057.

Longuet-Higgins, M.S., Stewart, R.W., 1964. Radiation stresses in water waves; a physical discussion, with applications. Deep-Sea Research 11, 529–562.

Mendez, F. J., M. Menendez, A. Luceno, and Losada, I. J., 2007. Analyzing monthly extreme sea levels with a time-dependent GEV model, J. Atmos. Oceanic Technol., 24(5), 894–911.

Mentaschi, L., Vousdoukas, M. I., Voukouvalas, E., Dosio, A., and Feyen, L., 2017. Global changes of extreme coastal wave energy fluxes triggered by intensified teleconnection patterns. Geophys. Res. Lett., 44, doi:10.1002/2016GL072488.

Michaelis, A.C., J. Willison, G.M. Lackmann, and W.A. Robinson, 2017: Changes in Winter North Atlantic Extratropical Cyclones in High-Resolution Regional Pseudo–Global Warming Simulations. J. Climate, 30, 6905–6925, https://doi.org/10.1175/JCLI-D-16-0697.1

Moss, R. H., and coauthors, 2010. The next generation of scenarios for climate change research and assessment. Nature, 463, 747-756.

Mousavi, M., J. Irish, A Frey, F. Olivera, and Edge, B., 2011. Global warming and hurricanes: the potential impact of hurricane intensification and sea level rise on coastal flooding. Climate Change, 104(3-4), 575-597.

National Oceanic and Atmospheric Adminstration (NOAA), National Data Buoy Center (NDBC), 2014. Data last accessed March 2016, www.ndbc.noaa.gov.

National Oceanic and Atmospheric Adminstration (NOAA), 2013. https://data.noaa.gov/dataset/2013-noaa-coastal-california-topobathy-merge-project-digital-elevation-model-dem

National Oceanic and Atmospheric Adminstration (NOAA), 2017. Tides & Currents, Center of Operational Products and Services, http://tidesandcurrents.noaa.gov.

NOAA/OAR/ESRL PSD, 2014. Sea surface temperature data: NOAA_OI_SST_V2 data provided by the, Boulder, Colorado, USA, from their Web site at http://www.esrl.noaa.gov/psd/

O'Reilly W.C., and Guza, R.T., 1993. Comparison of two spectral wave models in the Southern California Bight. Coastal Engineering, 19(3):263–282.

O'Reilly W.C., Guza, R.T., and Seymour, R.J., 1999. Wave prediction in the Santa Barbara Channel. Proc. 5th California Islands symposium, mineral management service, Santa Barbara CA, March 29–31.

O'Reilly, W.C., 1993. The southern California wave climate: effects of islands and bathymetry: Shore and Beach, v. 61, p. 14–19.

Pugh, D. T. 1987. Tides, Surges and Mean Sea-Level, John Wiley & Sons, Chichester, U. K.

Reynolds, R.W., N.A. Rayner, T.M. Smith, D.C. Stokes, and W. Wang, 2002. An improved in situ and satellite SST analysis for climate. J. of Climate, 15, 1609-1625.

Ris, R.C., Booij, N., and Holthuijsen, L.H., 1999. A third-generation wave model for coastal regions: Part II –Verification.: Journal of Geophysical Research, 104(C4), 7667-7682.

Roelvink, J.A., Reniers, A., van Dongeren, A.R., van Thiel de Vries, J.S.M., McCall, R., Lescinski, J., 2009. Modeling storm impacts on beaches, dunes and barrier islands. Coast. Eng. 56, 1133–1152

Rogers W., Kaihatu J., Hsu L., Jensen R., Dykes J., and Holland K., 2007. Forecasting and hindcasting waves with the SWAN model in the southern California Bight. Coastal Engineering 54(1):1–15

Rousseeuw, P.J., 1987. Silhouettes: a Graphical Aid to the Interpretation and Validation of Cluster Analysis". Computational and Applied Mathematics, 20: 53–65. doi:10.1016/0377-0427(87)90125-7

Ruggiero, P., Komar, P.D., McDougal, W.G., Marra, J.J., Beach, R.A., 2001. Wave runup, extreme water levels and the erosion of properties backing beaches. Journal of Coastal Research 17 (2), 407–419.

Ruggiero, P., Komar, P.D., Allan, J.C., 2010. Increasing wave heights and extreme value projections: The wave climate of the U.S. Pacific Northwest. Coastal Eng., 57, 5, 539-552.

Scripps Institute of Oceanography (SIO), University of California at San Diego, 2015a. Reanaysis and projection of winds and sea level pressures. Data not yet released.

Scripps Institute of Oceanography (SIO), University of California at San Diego. Coastal Data Information Program (CDIP), 2017. Last accessed March 2015. https://cdip.ucsd.edu/

Seiler, C. and Zwiers, F.W., 2016. How will climate change affect explosive cyclones in the extratropics of the northern hemisphere? Clim Dyn, 46: 3633.

Semedo, A.,Weisse, R., Behrens, R., Sterl, A., Bengtsson, L., Gunhter, H., 2013. Projection of global wave climate change toward the end of the twenty-first century. J. Climate, 26, 8269-8288.

Serafin, K. A., and P. Ruggiero, 2014. Simulating extreme total water levels using a time-dependent, extreme value approach, J. Geophys. Res. Oceans, 119, 6305–6329,

Serafin, K., Ruggiero, P. and Stockdon, H.F., 2017. The relative contribution of waves, tides, and non-tidal residuals to extreme total water levels on US West Coast sandy beaches. Geoph. Res. Lett., 44, 1839–1847.

Smith, J.M., M.A. Cialone, T.V. Wamsley, and T.O. McAlpin. 2010. Potential impact of sea level rise on coastal surges in southeast Louisiana. Ocean Engineering, 37(1), 37-47.

Solomon, S., D. Qin, M. Manning, Z. Chen, M. Marquis, K. B. Averyt, M. Tignor, and H. L. Miller, Eds., 2007. Climate Change 2007: The Physical Science Basis. Cambridge University Press, 996 pp

Stockdon, H.F., Holman, R.A., Howd, P.A., and Sallenger Jr., A. H., 2006. Empirical parameterization of setup, swash, and runup, Coastal Engineering, 53(7), 573-588.

Storlazzi, C.D., Griggs, G.B., 1998. The 1997–98 El Niño and erosion processes along the central coast of California. Shore and Beach, 66(3):12–17.

Sweet, W. V. and Park, J., 2014. From the extreme to the mean: Acceleration and tipping points of coastal inundation from sea level rise, Earth's Future, 2, doi:10.1002/2014EF000272.

Theuerkauf, E. J., Rodriguez, A. B., Fegley, S. R., and R. A. Luettich Jr., 2014. Sea level anomalies exacerbate beach erosion, Geophys. Res. Lett., 41, 5139–5147.

Tolman, H. L., Balasubramaniyan, B., Burroughs, L. D., Chalikov, D. V., Chao, Y. Y., Chen H. S., Gerald, V.M., 2002. Development and implementation of wind generated ocean surface wave models at NCEP. Weather and Forecasting, 17(2), 311-333.

Ulbrich, U., J.G. Pinto, H. Kupfer, G.C. Leckebusch, T. Spangehl, and M. Reyers, 2008: Changing Northern Hemisphere Storm Tracks in an Ensemble of IPCC Climate Change Simulations. J. Climate, 21, 1669 -1679.

Wood AW, Leung LR, Sridhar V, Lettenmaier DP. 2004. Hydrologic implications of dynamical and statistical approaches to downscaling climate model outputs. Climatic Change 62: 189–216.

Yin, J.H., 2005. A consistent poleward shift of the storm tracks in simulations of 21st century climate. Geophys. Res. Lett. 32, L18701.

Figures

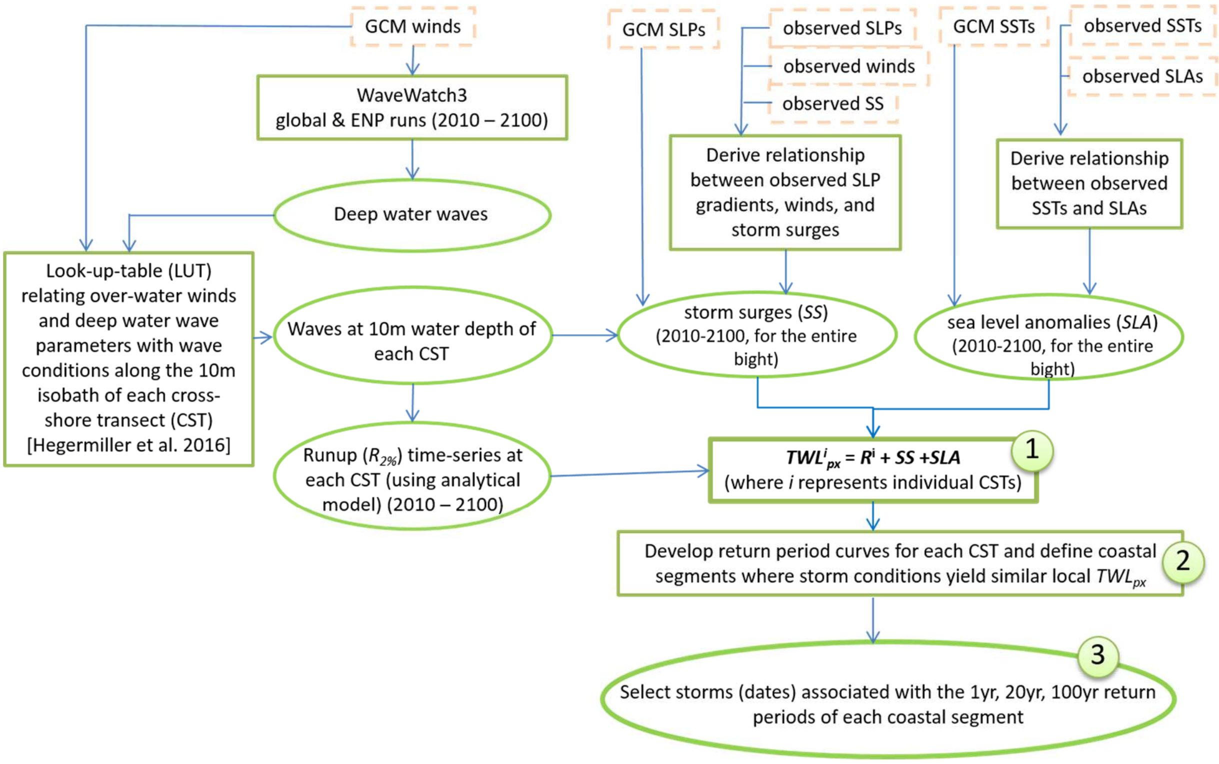

Figure 1. Flowchart summarizing the workflow used to determine TWL proxies at the coast and selecting future storm events for detailed deterministic modeling of local extreme flood events. Dashed and solid rectangles refer to input data and computations + outputs, respectively; ovals and circles refer to outputs. Numbered items 1 through 3 highlight results discussed in detail in the text.

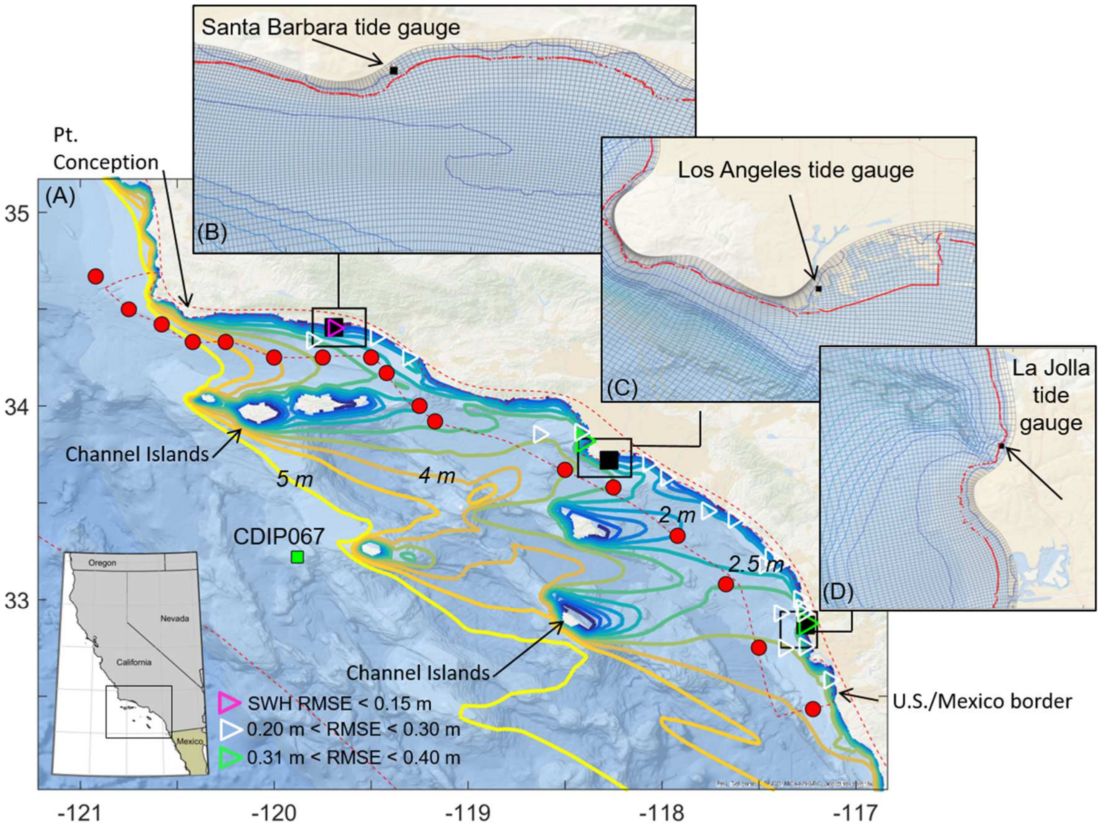

Figure 2. Overview of the study area and wave model grid and boundaries. (A) Southern California Bight study area with bathymetry (background image: Esri, DeLorme, GEBCO, NOAA NGDC and others). Red circles and dashed red line indicates SWAN model grid bounds and U.S. Army Corps of Engineers Wave Information Study (WIS) boundary forcing points used to compute a 30-yr hindcast of nearshore waves. Root-mean square errors between model outputs and observations are shown with the colored triangles. CDIP067 (green square) indicates offshore location where winds and deep-water waves are related to nearshore wave conditions via a look-up-table. Colored contours depict wave heights simulated with the same grid nested in a larger grid that extends past the continental shelf (bounds partially shown with black dashed line, *SWH* = 6 m, T_p = 13s, D_p = 288°) to illustrate shadowing and blocking of wave energy by the Channel Islands. (B - D) Zoom-in of the nearshore grid in the vicinity of Santa Barbara, Los Angeles, and La Jolla. Tide gauge locations used in the study are shown with black squares. Red dots (cross-shore transect points) show locations along the 10 m isobath where total water level proxies are computed. cross-shore transects are numbered from 1 near the U.S./Mexico border to 4,802 near Pt. Conception. Bathymetric contours are at 50 m intervals.

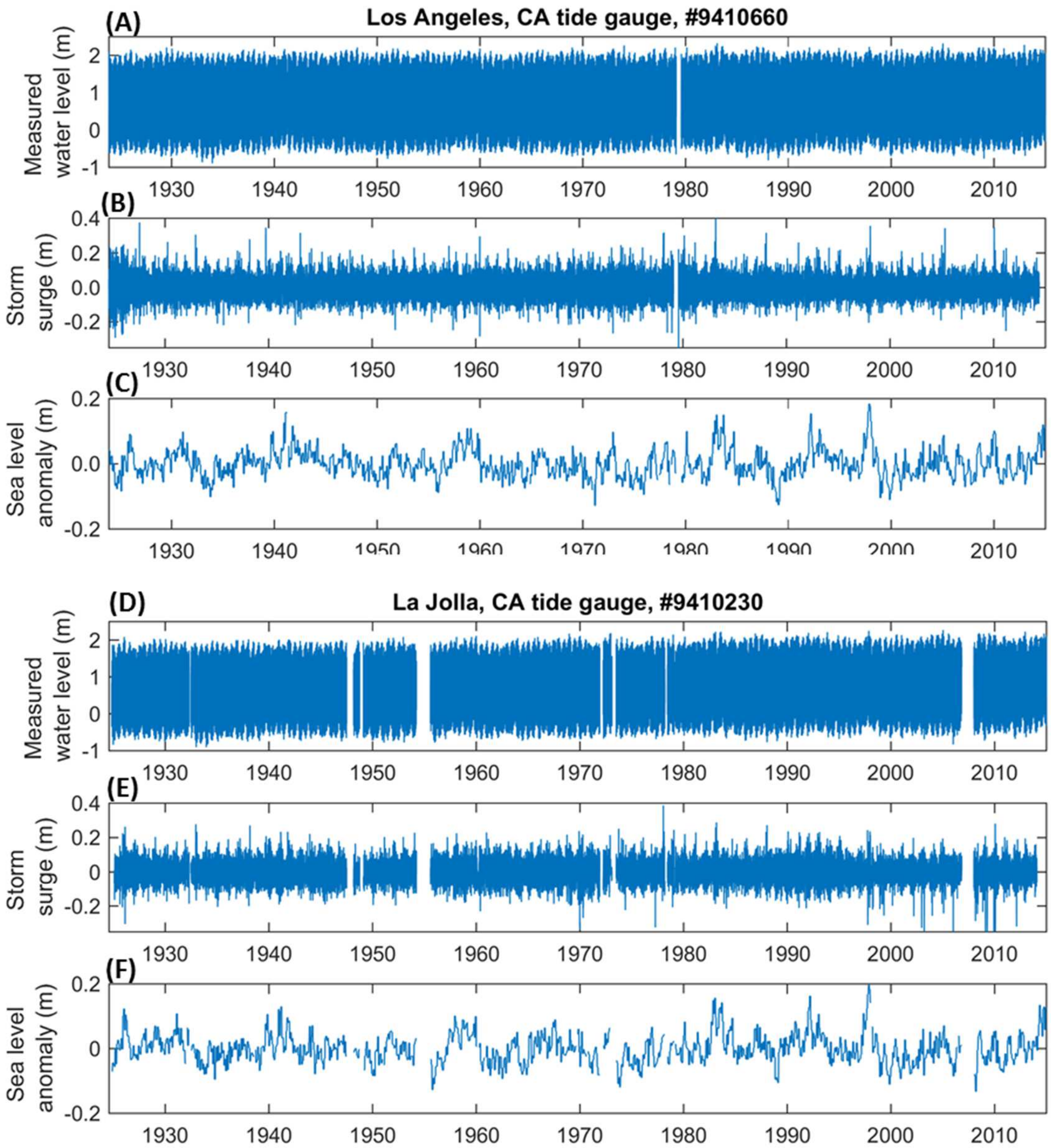

Figure 3. Measured water levels and decomposed time-series of storm surge and of mean monthly sea level anomalies. (A-C) Los Angeles tide gauge #9410660; (D-F) La Jolla tide gauge #9410230. Measured water levels in (A) and (D) are referenced to vertical datum NAVD88.

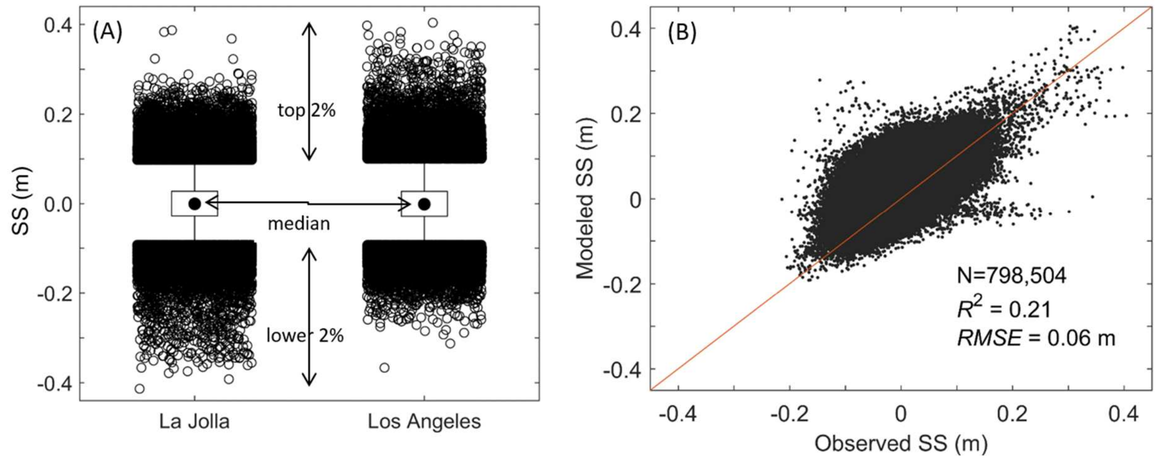

Figure 4. Measured and modeled storm surge levels. (A) Observed storm surge levels at La Jolla and Los Angeles tide gauges (01 Aug 1924 through 31 Dec 2014). Filled circles are the median, upper and lower edges of the rectangles are the 25th and 75th percentiles, and open circles are extremes above and below the 98th and 2nd percentiles. (B) Measured and computed (using Eq. 2) storm surge levels at the Los Angeles tide gauge (01 Jan 1980 through 31 Dec 2010).

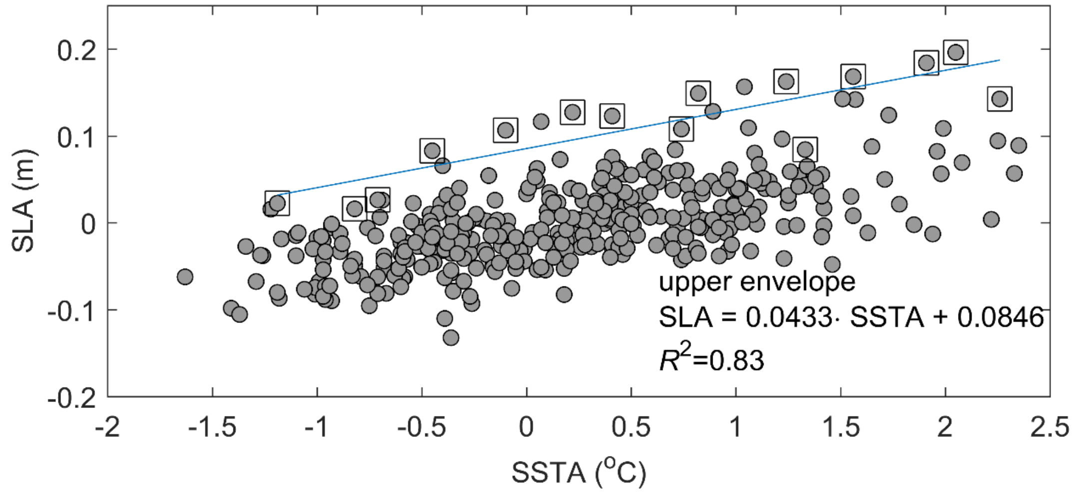

Figure 5. Sea level anomalies (SLA) and sea surface temperature anomalies (SSTAs) at the La Jolla tide gauge (1981-2014) and linear fit through the upper envelope (highest value at 0.25° bins shown with squares).

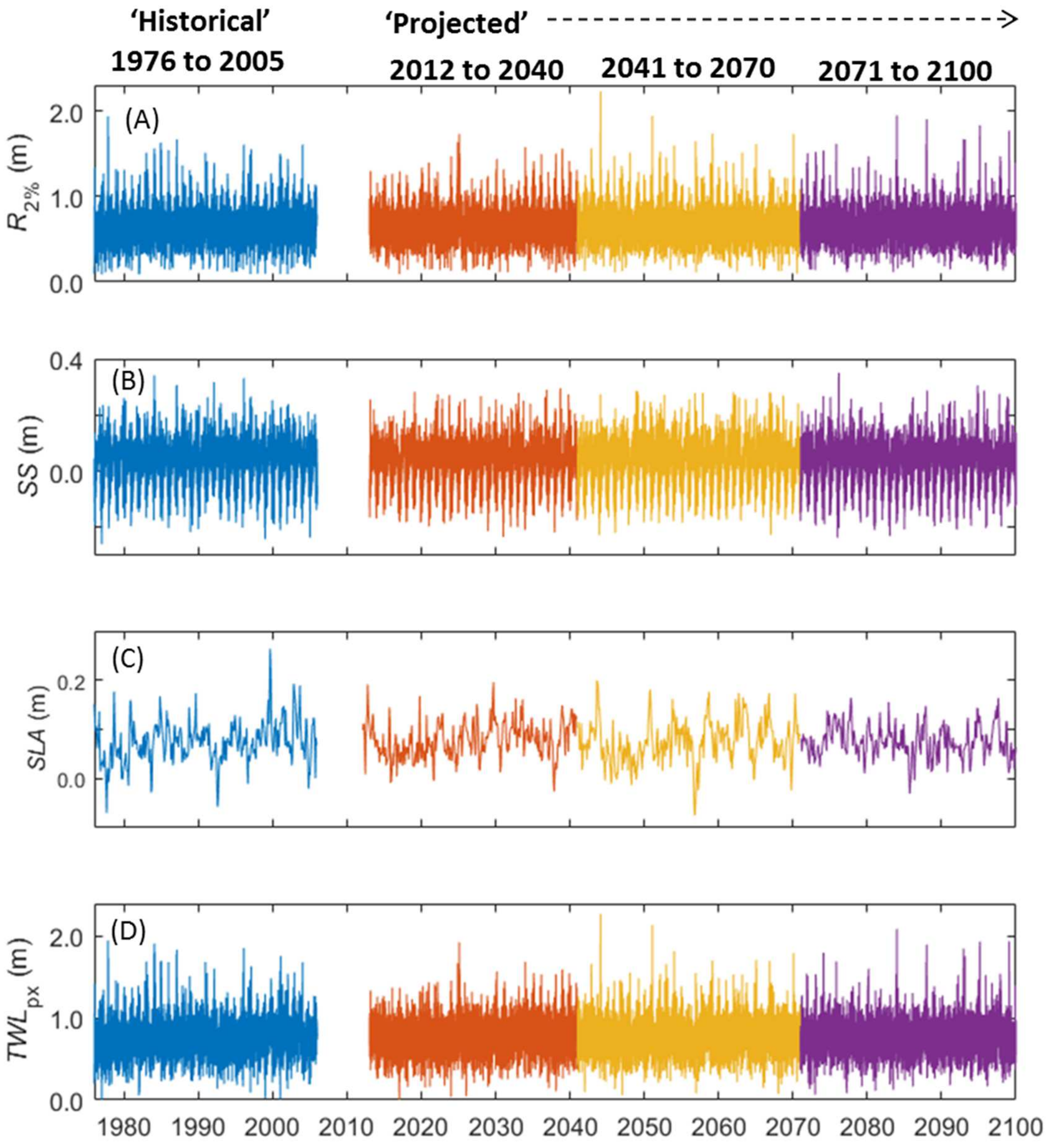

Figure 6. Bight-wide averaged time-series of historical and projected nearshore coastal water levels using downscaled GFDL-ESM2M, RCP4.5. (A) Wave runup, (B) storm surge, (C) sea level anomalies, and (D) total water level proxies equal to the summation of all three components in A through C.

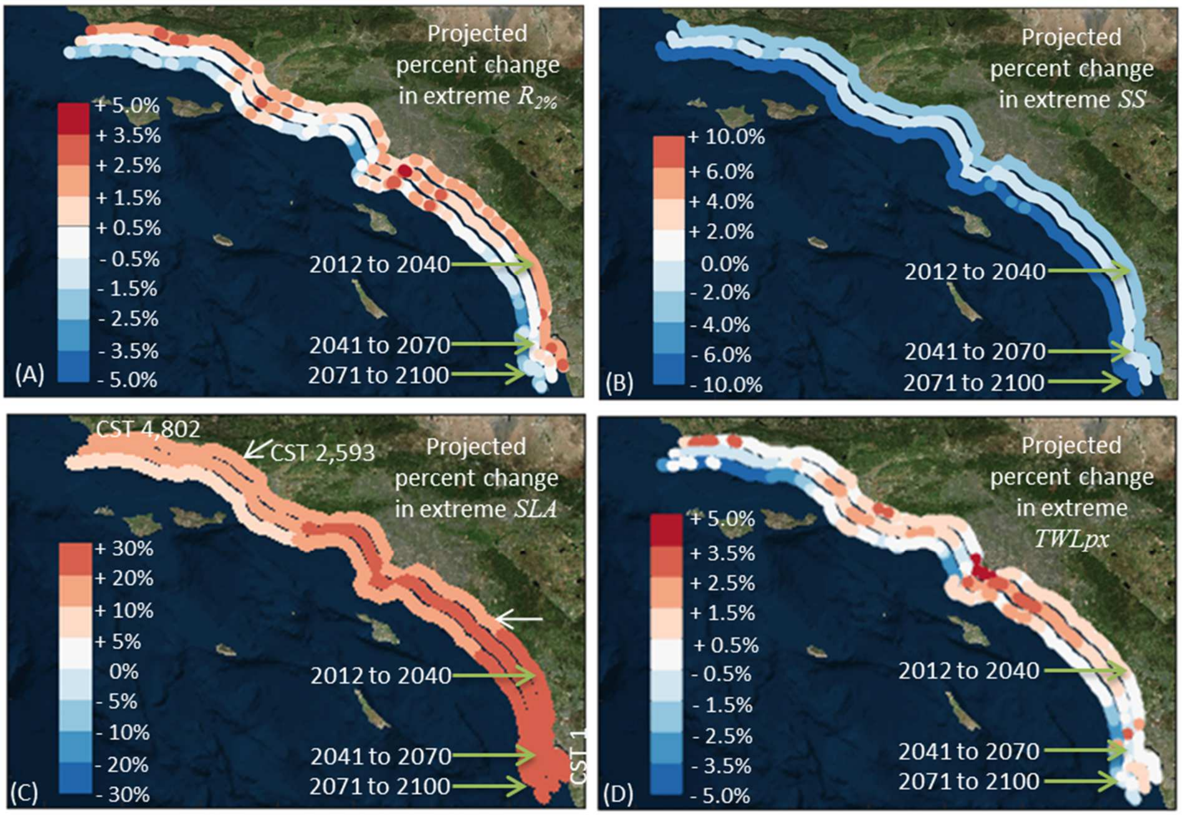

Figure 7. Percent change of extremes between three 30-year projected time-slices and the historical time-period (1976 – 2005). Percent change of the 98th percentile (A) wave runup assuming a constant foreshore slope of 0.03, (B) storm surge, (C) sea level anomalies, and (D) *TWLpxs*, the summation of all components.

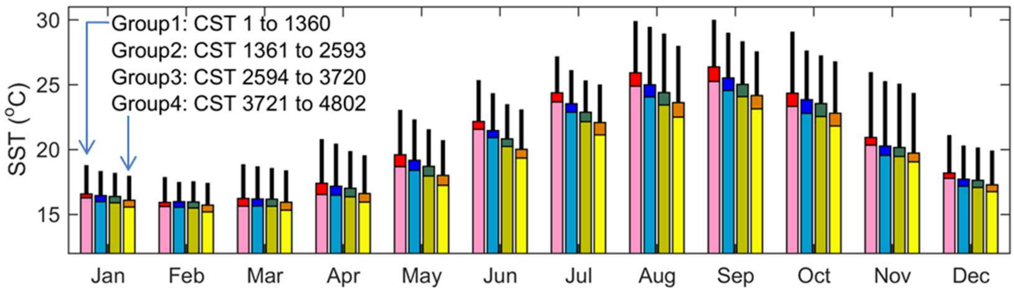

Figure 8. GCM modeled monthly mean SSTs within the Southern California Bight. Four regions associated with the GCM grid points are defined from south (Group 1) to north (Group 4). Historical (1976-2005) and projected (2012-2100) monthly means are shown with lighter and darker colored bars, respectively. Vertical black lines depict projected monthly maxima.

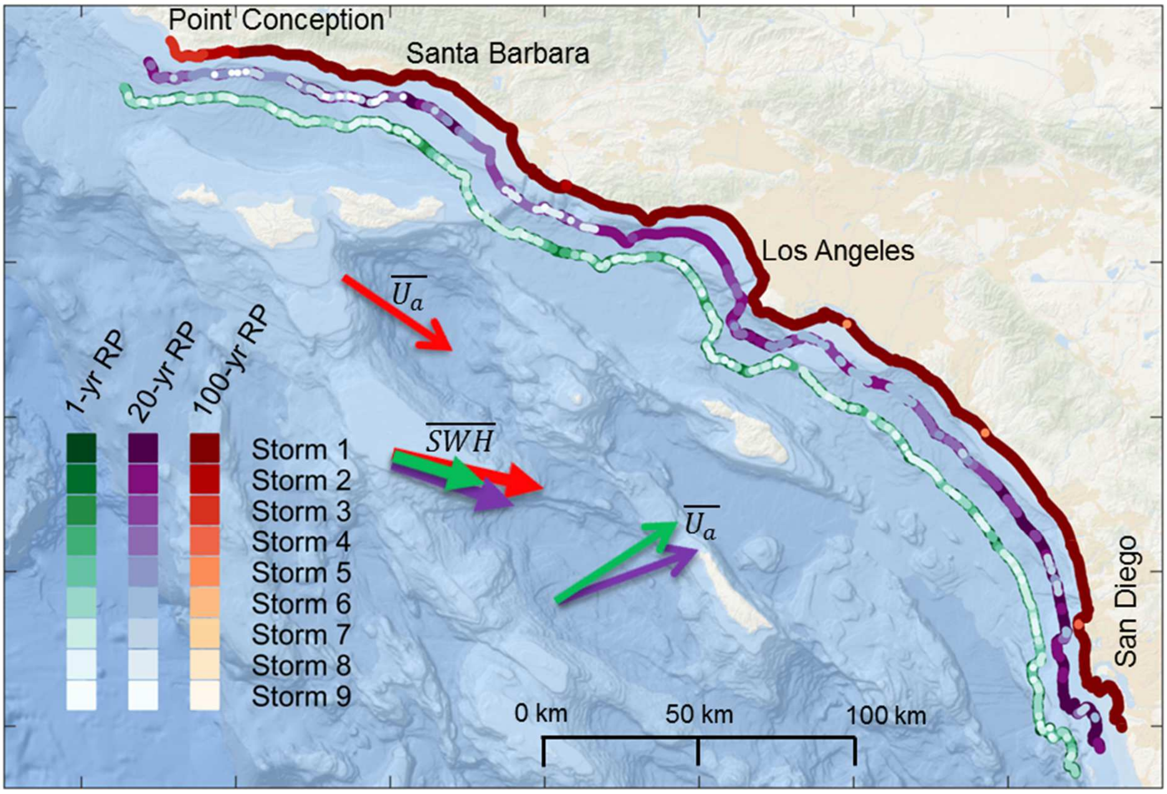

Figure 9. Identification of coastal cells that respond similarly to region-wide storms. Large colored arrows show the weighted mean (Table 4) offshore wave heights and winds for the 1-yr, 20-yr and 100-yr return period coastal storms.